Available online at www.sciencedirect.com

ScienceDirect

Ceramics International 40 (2014) 15859–15874

CERAMICS INTERNATIONAL

www.elsevier.com/locate/ceramint

Role of Cr additions in enhancing wear and oxidation resistance of $(Mo_{1-x}Cr_x)Si_2$ nanocrystalline films

Jiang Xu[a,b,*], ZhengYang Li[c], Paul Munroe[d], Zong-Han Xie[e,b]

[a]Department of Material Science and Engineering, Nanjing University of Aeronautics and Astronautics, 29 Yudao Street, Nanjing 210016, PR China
[b]School of Mechanical & Electrical Engineering, Wuhan Institute of Technology, 693 Xiongchu Avenue, Wuhan 430073, PR China
[c]Institute of Mechanics, Chinese Academy of Sciences, Beijing 100190, People's Republic of China
[d]School of Materials Science and Engineering, University of New South Wales, NSW 2052, Australia
[e]School of Mechanical Engineering, University of Adelaide, SA 5005, Australia

Received 9 July 2014; received in revised form 19 July 2014; accepted 21 July 2014
Available online 29 July 2014

Abstract

In order to explore the effects of Cr alloying on the wear and oxidation resistance of $MoSi_2$ films, four kinds of $(Mo_{1-x}Cr_x)Si_2$ ($x=0$, 0.05, 0.10 and 0.15) nanocrystalline films of differing Cr contents were fabricated onto Ti_6Al_4V substrates by a double cathode glow discharge apparatus. The microstructure features of the as-deposited films were characterized by X-ray diffraction (XRD), field-emission scanning electron microscopy (FESEM) and transmission electron microscopy (TEM). The hardness and elastic modulus of the $(Mo_{1-x}Cr_x)Si_2$ nanocrystalline films were evaluated by nano-indentation. The dry sliding wear properties of the as-deposited films sliding against GCr15 rolling bearing steel were studied using a ball-on-disc type tribometer at room temperature. The results showed that the friction coefficients and specific wear rates of the $(Mo_{1-x}Cr_x)Si_2$ nanocrystalline films decreased with increasing Cr content in the films. The oxidation behavior of the $(Mo_{1-x}Cr_x)Si_2$ nanocrystalline films was investigated at 500 °C under cyclic oxidation conditions in air for exposure time of 100 h. The oxidation kinetics of the films was found to obey a subparabolic behavior, and three Cr-containing $MoSi_2$ films showed a much lower weight gain and the oxidation rate constant as compared to the monolithic MoSi2 film during a 100 h exposure. Surface morphologies, phase constituents and electrochemical behavior of the oxide scales formed on the $(Mo_{1-x}Cr_x)Si_2$ nanocrystalline films were characterized using FESEM, XRD and electrochemical-impedance spectroscopy (EIS). The electrochemical results revealed that the structure of the oxide scales changed from a homogeneous and dense structure to a duplex structure consisting of a porous outer layer and a denser inner layer. The overall resistance of the oxide scales depended strongly on both the oxidation time and Cr content in the films.

Keywords: Molybdenum silicides; Oxidation behavior; Friction and wear; Electrochemical impedance spectroscopy

1. Introduction

In the past few decades, considerable work has been undertaken worldwide to develop new material systems that could offer superior performance to Ni-base superalloys for high temperature structural applications in aerospace industries for further improvement in the energy efficiency [1,2]. Among the various refractory metal silicides that have been currently considered to be suitable candidates, molybdenum disilicide ($MoSi_2$) stands out owing to good mechanical strength, high thermal conductivity and moderate coefficient of thermal expansion [3]. However, its limited room temperature mechanical properties and poor oxidation resistance at moderate temperatures have hindered its practical application. In terms of oxidation behavior, at temperature above 800 °C, $MoSi_2$ exhibits good oxidation resistance via the formation of a thin, continuous, adherent glass silica layer, which serves as a physical barrier between $MoSi_2$ material and adjacent atmosphere by preventing the diffusion of oxygen. At temperatures around 500 °C, however, $MoSi_2$ undergoes severe oxidation, referred to

*Corresponding author at: Department of Material Science and Engineering, Nanjing University of Aeronautics and Astronautics, 29 Yudao Street, Nanjing 210016, PR China. Tel./fax: +86 02552112626.
E-mail address: xujiang73@nuaa.edu.cn (J. Xu).

http://dx.doi.org/10.1016/j.ceramint.2014.07.114
0272-8842/

as "pest oxidation", leading to the disintegration of the material into powder [4]. Significant research activity has been focused on this issue attempted to understand and control the pesting phenomenon of $MoSi_2$. The pest oxidation of $MoSi_2$ was found to be intimately associated with environmental factors like oxidation temperature [5] and atmosphere [6]. As described above, oxidation rates (and presumably controlling mechanisms) change with increasing temperature, and the pest phenomenon only occurs in air in the temperature around 500 °C. This may be due to the fact that the low Si diffusion rate in $MoSi_2$ at moderate temperatures, simultaneous oxidation of Mo and Si would retard the formation of a silica protective layer [5]. Although the mechanisms proposed for the pesting of $MoSi_2$ so far are still open to question, previous studies also indicated that the accelerated oxidation of $MoSi_2$ was closely related to material factors such as microstructure and porosity [5–8]. For example, Bertiss et al. [7] reported that cast $MoSi_2$ containing microcracks underwent accelerated oxidation and fragmentation, whereas hot isostatically pressed and single crystal $MoSi_2$ without microcracks, also underwent accelerated oxidation but did not fragment. Westbrook et al. [8] proposed that the catastrophic nature of the pest oxidation was attributed to the preferential inter-granular diffusion of a gaseous element, coupled with grain boundary embrittlement. Many other researchers indicated that the most severe oxidation occurred in pre-existing cracks and/or pores, and the internal stresses produced from oxide growth in these defects resulted in disintegration of the sample to powders [9,10]. Therefore, the operating temperatures and defects have been identified to be the most critical factors affecting the catastrophic oxidation behavior of $MoSi_2$. To date, the main approaches used to improve the poor oxidation resistance of $MoSi_2$ at moderate temperatures have included either incorporating of ceramic phase, such as Al_2O_3 [11] and Si_3N_4 [12], into the $MoSi_2$ matrix or adding alloying elements, like Ti, Cr, Zr, and Al [4,13]. Because Cr has stronger affinity for oxygen than Si, the addition of Cr to $MoSi_2$ shows a beneficial effect on oxidation resistance by reducing the oxygen flux toward the oxide- $MoSi_2$ interface [14].

The electrochemical corrosion in aqueous solution and high-temperature oxidation of metals and alloys at elevated temperatures share similar electrochemical traits, i.e., the metal transforms into metal ions accompanied by electron transfer. As such, both the oxidation-resistance at high temperature and corrosion resistance in aqueous solution rely heavily on the protective ability of oxide layers formed on the metal surface. The protective potential of an oxide layer is dependent on its ability to obstruct the transport of cations, anions, or their vacancies across itself [15]. Thus, the corrosion resistance of the passive layers in aqueous solution has the same root as the resistance of the oxide layers against high-temperature oxidation. Furthermore, the potential application of $MoSi_2$ is for hot-section components of aircraft gas turbine engines, such as vanes. The presence of defects is also detrimental to the corrosion resistance of the oxide layers in aqueous solution, due to the speeding up chemical reactions through penetration of electrolyte into the oxide layer. $MoSi_2$, with oxide scales on its surface after operation at high temperature, may suffer from corrosive attack in aggressive environments (e.g. chlorine ions containing media induced by saline marine air) [16]. Therefore, from a practical standpoint, an in-depth knowledge of corrosion resistance of its oxide scale in containing chloride anions medium is necessary. Moreover, from a tribological perspective, $MoSi_2$ can potentially be regarded as an attractive wear resistant and anti-friction surface coating material because of its inherently high hardness [17].

Electrochemical-impedance spectroscopy (EIS) is a simple, effective and non-destructive technique, which has been extensively used to characterize the electrical properties of passive film on metal substrates in an aqueous solution and high temperature oxide layers on zircaloy and different stainless steels [18–20]. Besides, EIS measurement has the advantage of a high sensitivity in detecting defects such as pores, channels, and cracks inside the oxide scale. In the present study, the low-temperature cyclic oxidation behavior of the $(Mo_{1-x}Cr_x)Si_2$ nanocrystalline films with differing Cr contents was investigated by weight gain measurements and electrochemical-impedance spectroscopy (EIS), with a focus on the effect of the Cr additions on the oxidation resistance of the $(Mo_{1-x}Cr_x)Si_2$ nanocrystalline films. In addition, the influence of Cr additions on mechanical properties and wear resistance of the $(Mo_{1-x}Cr_x)Si_2$ nanocrystalline films was also examined and clarified.

2. Experimental details

2.1. Preparation of nanocrystalline $Mo(Si_{1-x}Al_x)_2$ films

Specimens (∅ 40 mm × 4 mm) used as the substrates were cut from a Ti–6Al–4V alloy rod. The nominal composition of this alloy in wt% is: Al, 6.04; V, 4.03; Fe, 0.3; O, 0.1; C, 0.1; N, 0.05; H, 0.015 and the balance, Ti. Before coating deposition, the substrates were polished successively using SiC papers and 1 μm diamond paste. The polished substrates were then ultrasonically cleaned in acetone, alcohol, distilled water and then dried. Four $(Mo_{1-x}Cr_x)Si_2$ (x=0, 0.05, 0.10 and 0.15) nanocrystalline films were deposited on mirror-polished Ti–6Al–4V substrates by a double cathode glow discharge equipment using four targets with different stoichiometric ratios (i.e., $Mo_{25}Si_{75}$, $Mo_{20}Cr_3Si_{75}$, $Mo_{19}Cr_6Si_{75}$ and $Mo_{15}Cr_{10}Si_{75}$), respectively. The reason for the difference in the composition of the targets and the deposited films is that the composition of the films is related not only the alloy content of target materials, but also the relative sputtering yields of the alloying elements in the targets. Furthermore, diffusion of alloying elements at the interface between the films and substrate will also affect the composition of the deposited films. Inside the chamber, one cathode is used as the target and the other as the substrate, as described elsewhere [21]. Optimized deposition parameters for the films were as follows: base pressure, 4×10^{-4} Pa; target electrode bias voltage, −900 V; substrate bias voltage, −300 V; substrate temperature, 800 °C; working pressure (Ar gas, 99.99% purity), 35 Pa; parallel distance between the source electrode and the substrate, 15 mm and treatment time of 5 h. The sputtering targets were fabricated from ball-milled Mo (99.99% purity), Cr (99.99% purity) and Si

powders (99.99% purity) by employing cold compaction under a pressure of 600 MPa.

2.2. Phase and microstructure characterization

Phase identification of the as-deposited films was performed using a D8ADVANCE X-ray diffraction (XRD) machine with Cu target ($\lambda = 0.15406$ nm), radiation operated at 35 kV and 40 mA. X-ray data were collected using a 0.1° step scan with a count time of 1 s. The as-deposited films were etched in Kroll's reagent (10 ml HNO_3, 4 ml HF and 86 ml distilled water) for 20–30 s. A field emission scanning electron microscope (FE-SEM, Sirion 400NC, FEI Company) equipped with an energy-dispersive X-ray spectrometer (EDX), was used to observe the cross-sectional morphology and chemical composition of the as-deposited films. Transmission electron microscopy (TEM) images were performed using a JEOL JEM-2010 at an accelerating voltage of 200 kV. Plan-view TEM samples were cut from the outermost part of the films and prepared using single-jet electrochemical polishing technique starting from the untreated side of the substrates.

2.3. Nanoindentation and wear tests

The hardness and Young's modulus of the as-deposited films were measured using a nanoindentation tester (NHT) equipped with a Berkovich tip (CSEM Instruments). This system comprised two components: a measuring head for performing nanoindentation tests and an optical microscope for selecting a specific site prior to indentation and for checking the indents after testing. The system has load and displacement resolutions of 10 mN and 1 nm, respectively. Fused silica was used as the standard sample for the initial tip calibration. Indentation was performed by driving the indenter at a constant loading rate of 40 mN/min into the specimen surface with the maximum applied load of 20 mN. The standard analysis procedure, proposed by Oliver and Pharr [22], was used to determine the hardness of the specimens from the unloading curve. For each type of sample, nanoindentation tests were conducted at five different locations to ensure repeatability of the experimental data. Dry wear tests were performed with an HT-500 ball-on-disc tribometer, in which, a disc sample of as-deposited films were sliding against an 3 mm diameter ball made of GCr15 bearing steel (nominal hardness 840 HV). The wear tests were carried out at ambient temperature with the normal loads of 2.3, 3.3, 4.3 and 5.3 N, and the sliding speed of the counterpart ball was 22 cm/s with a track diameter of 6 mm. The test duration was 30 min, which corresponded to a 396 m sliding distance. The friction coefficient was monitored on-line during the tests. The worn volume loss was assessed by calculating the cross-sectional areas of wear tracks developed on the surface of the samples, after measuring their width and depth using a MicroXAM^{TM} non-contact optical profilometer (ADE Phase-Shift, USA). The morphology of worn surfaces was also observed by SEM.

2.4. Cyclic oxidation test

Cyclic oxidation tests were conducted at 500 °C in air (1 atm) for a maximum of 100 cycles. The specimens were held in a high-purity alumina crucible (the crucible had been heated at 600 °C to achieve a constant mass) and inserted into the center of a muffle furnace. The furnace hot zone was maintained at the designated temperature during the entire duration of test. For one thermal cycle, oxidation inside the furnace and cooling in ambient air were 60 and 10 min. After the desired amount of time (10 h), the specimens were withdrawn from the furnace, cooled in a desiccator, and then weighed using an electronic balance with an accuracy of 0.01 mg. Cumulative weight changes per unit area of samples were calculated and reported as a function of oxidation time. After cyclic oxidation, the surface morphology, chemical composition and phase constitution of the oxide scales formed on the specimens were characterized using SEM, EDX and XRD.

2.5. Electrochemical measurements

Electrochemical measurements were carried out using a CHI660C electrochemical analyzer. Each specimen oxidized for various times at 500 °C was used as a working electrode and was connected to a conducting wire and then embedded with non-conducting epoxy resin leaving a square surface of approximately 1 cm^2 exposed to the solution. The electrolyte used was a 3.5 wt% NaCl solution open to the air, which was prepared from analytical grade reagents and distilled water. A standard three-compartment cell was used with a saturated calomel electrode (SCE) and a platinum electrode as a reference and counter electrode, respectively. Throughout this paper, all electrode potentials are referred to the SCE. At each test condition, the open circuit potential (OCP) was continuously monitored for 3600 s to obtain a stable electrochemical condition, then EIS measurements were conducted over the frequency range of 100 kHz to 10 mHz, with an acquisition of

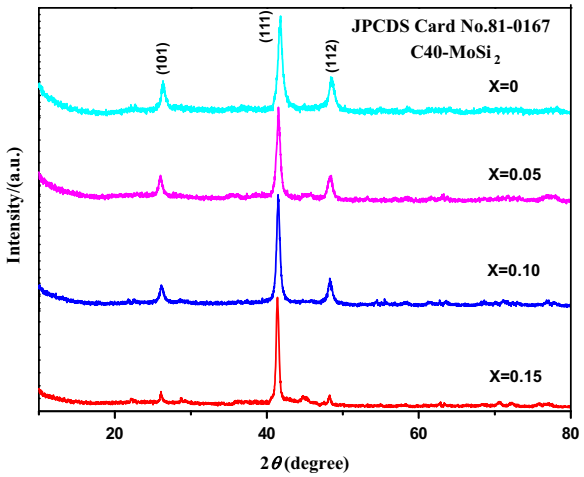

Fig. 1. XRD patterns recorded from the as-deposited $(Mo_{1-x}Cr_x)Si_2$ films.

12 points per decade of frequency, at respective OCPs, and an amplitude of the AC signal of 10 mV.

3. Results and discussion

3.1. Microstructures and phase analysis

Fig. 1 shows the X-ray diffraction patterns taken from the four as-deposited $(Mo_{1-x}Cr_x)Si_2$ ($x=0$, 0.05, 0.10 and 0.15) films. The XRD spectra of the as-deposited films are characterized by a set of broad peaks from the (101), (111) and (112) planes for the hexagonal C40-structured $MoSi_2$ (JCPDS card file no. 81-0167), indicating that all the as-deposited films consist of a single $(Mo_{1-x}Cr_x)Si_2$ phase. The strong intensity of C40 $MoSi_2$ (111) peak located at 41.36° indicates the as-deposited films show a strong (111) oriented texture. With increasing Cr addition, the diffraction peak positions shifted towards higher 2θ values with respect to the powder diffraction file data for the binary C40 $MoSi_2$, suggesting that a solid solution of Cr into the $MoSi_2$ reduces the lattice parameter due to the smaller atomic radius of Cr compared to Mo.

Fig. 2 shows typical cross-section SEM micrographs of the as-deposited $(Mo_{1-x}Cr_x)Si_2$ ($x=0$ and 0.05) films. It is evident that the as-prepared films exhibit a homogeneous dense structure without any visible structural flaws and they are tightly adhered to the substrate materials. By a combination of the XRD results and EDS analysis, the microstructure of the as-deposited films was characterized into two uniform layers, namely, an outer deposited layer and an inner diffusion layer. The 20 μm thick outer deposited layer has a molar ratio of Mo (or Mo+Cr) to Si close to 0.5 across its entire depth, indicating that the as-deposited layer is composed of single $MoSi_2$ phase. The underlying diffusion layer, composed mostly of Ti, Cr and Mo elements, can be further divided into a β phase layer and a α″/α′-Ti layer, from outside to inside depending on the Mo content in the diffusion layer, consistent with observations reported elsewhere [23]. Fig. 3 shows representative plan-view TEM bright-field/dark-field images and the corresponding selected area electron diffraction (SAED) pattern taken from the outer layers of the $(Mo_{0.95}Cr_{0.05})Si_2$ film. It can be seen from Fig. 3 that the microstructure of the outer layer consists of equiaxed grains

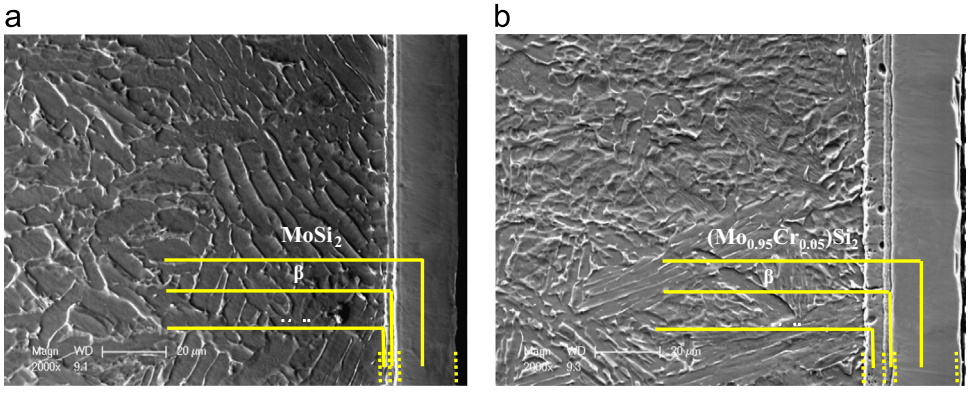

Fig. 2. Cross-sectional SEM images of the as-deposited $(Mo_{1-x}Cr_x)Si_2$ ($x=0$ and 0.05) films.

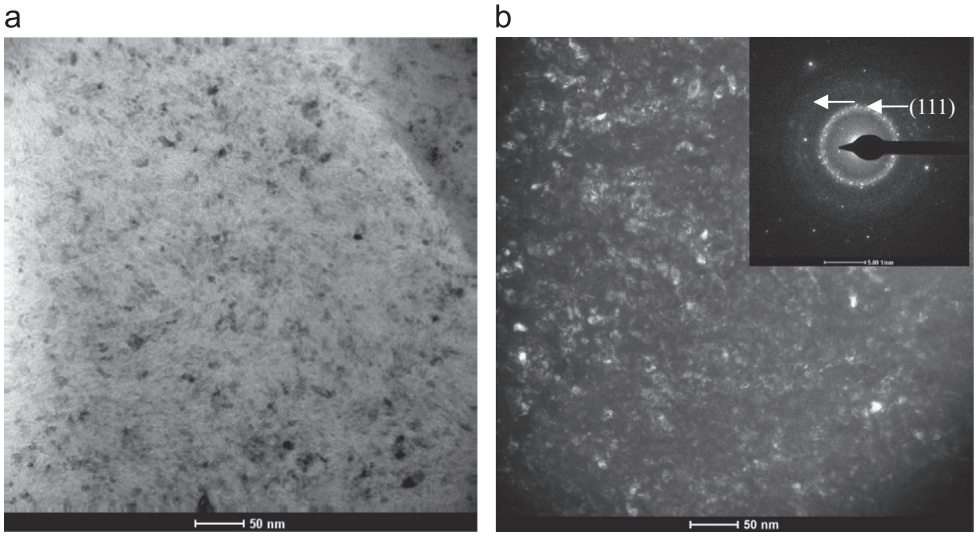

Fig. 3. (a) Bright-field and (b) dark-field TEM images with the corresponding selected area electron diffraction (SAED) pattern taken from the outer layers of the deposited $(Mo_{0.95}Cr_{0.05})$ Si_2 film.

with an average grain size of ~15 nm. The intense $MoSi_2$ (111) reflection provides further evidence that the $(Mo_{0.95}Cr_{0.05})Si_2$ film exhibits a strong (111) preferred orientation.

3.2. Nanoindentation test

Typical load–displacement (p–h) curves for the four $(Mo_{1-x}Cr_x)Si_2$ films obtained from instrumented nanoindentation under a maximum load of 20 mN are presented in Fig. 4 (a) and the resulting hardness and elastic modulus values are plotted in Fig. 4(b). As shown in Fig. 4(a), the largest indentation depth and residual depth are inversely proportional to Cr content in the films. It is generally accepted that for thin hard coatings on ductile substrates, if the indentation depth is lower than 10% of the films thickness, the contribution to mechanical properties from the substrate is negligible. The hardness and elastic modulus of the four $(Mo_{1-x}Cr_x)Si_2$ films monotonically increase with increasing Cr content in the films, suggesting that alloying C40-structured $MoSi_2$ with Cr results in solid solution hardening. The presence of solid-solution softening or hardening is commonly explained in terms of variations in Peierls potentials and in dislocation core structures through alloying. It should be pointed out that the addition of C40 disilicide forming elements, such as Cr and Al, has the opposite influences on $MoSi_2$ with both $C11_b$ and C40 structures. Solid-solution softening occurs by alloying $C11_b$-structured $MoSi_2$ with ternary elements that form a C40 disilicide, such as Nb and Al, because the addition of C40 disilicide forming elements reduce energies of stacking faults on {110} and Peierls stress [24,25]. Conversely, the addition of C40 disilicide forming elements to C40-structured $MoSi_2$ increases the Peierls stress and hence lowers dislocation mobility, leading to solid-solution hardening [26].

3.3. Friction and wear

The ball-on-disc configuration, which has been used to simulate wear process that occurs in dynamically loaded components such as bearings, gears and crankshafts, was applied to evaluate the wear resistance of the specimens. The variation of friction coefficient as a function of sliding time for the four $(Mo_{1-x}Cr_x)Si_2$ films sliding against GCr15 steel balls at different applied normal loads is plotted in Fig. 5. It can been seen that the friction coefficients increase rapidly during a short running-in period, and subsequently reach steady-state value exhibiting a narrow range of fluctuation. The steady-state friction coefficients for the four $(Mo_{1-x}Cr_x)Si_2$ films decrease with both increasing normal load and Cr concentration, indicating that Cr alloying is beneficial in improving the friction behavior of $MoSi_2$ presumably by forming an easily sheared lubricating surface layer. Fig. 6 displays the variation of specific wear rates of the four $(Mo_{1-x}Cr_x)Si_2$ films as a function of applied normal load after a sliding distance of 396 m at room temperature. Over the investigated range of loads, the specific wear rates are of the order of 10^{-6} mm^3/(N m), and increase with the applied normal loads for all of tested samples. Under identical normal loads, the specific wear rates of the as-deposited films decrease with increasing Cr content.

Fig. 7 shows SEM images of the worn surface morphologies of the four $(Mo_{1-x}Cr_x)Si_2$ films sliding against GCr15 steel balls under a normal loads of 5.3 N. As shown in Fig. 7(a), many shallow parallel grooves formed through plowing action are visible on the worn surface of the $MoSi_2$ film, and at the higher magnification (Fig. 7(b)), a large area of flaking with some micro-cracks can be observed. With increasing the amount of Cr content, the worn surfaces of the three Cr-containing $MoSi_2$ films gradually become smoother (Fig. 7(c)–(e)), showing no sign of flaking or micro-cracks, especially for the $(Mo_{0.85}Cr_{0.15})Si_2$ film. EDS analysis of the worn surface of the $MoSi_2$ film and the $(Mo_{0.85}Cr_{0.15})Si_2$ film indicates the presence O, Mo, Si, Cr and Fe elements peaks in the EDS spectra, as shown in Fig. 8. EDX analysis of the worn surfaces suggests the formation of a mixed oxide layer on the films induced by tribochemical reactions during the dry sliding wear process. This presumably because under the frictional heat generated at the interface between the tribo-couple, the nanocrystalline films are liable to react with oxygen to form a mixed oxide layer of Mo, Cr and Si. The presence of an amount of Fe (and an amount of Cr for the worn surface of the

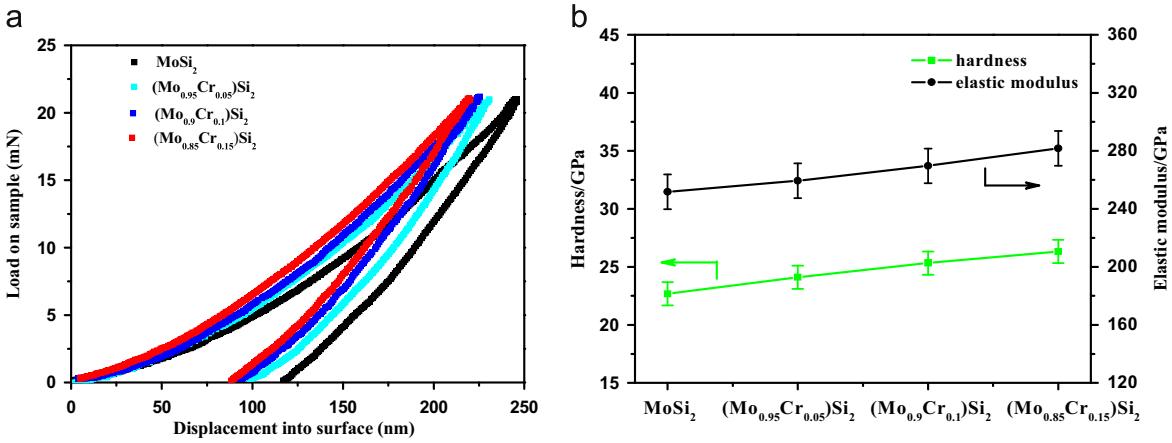

Fig. 4. (a) Load–displacement curves for the four $(Mo_{1-x}Cr_x)Si_2$ films, and (b) elastic modulus and hardness values as a function of Cr content for the four $(Mo_{1-x}Cr_x)Si_2$ films.

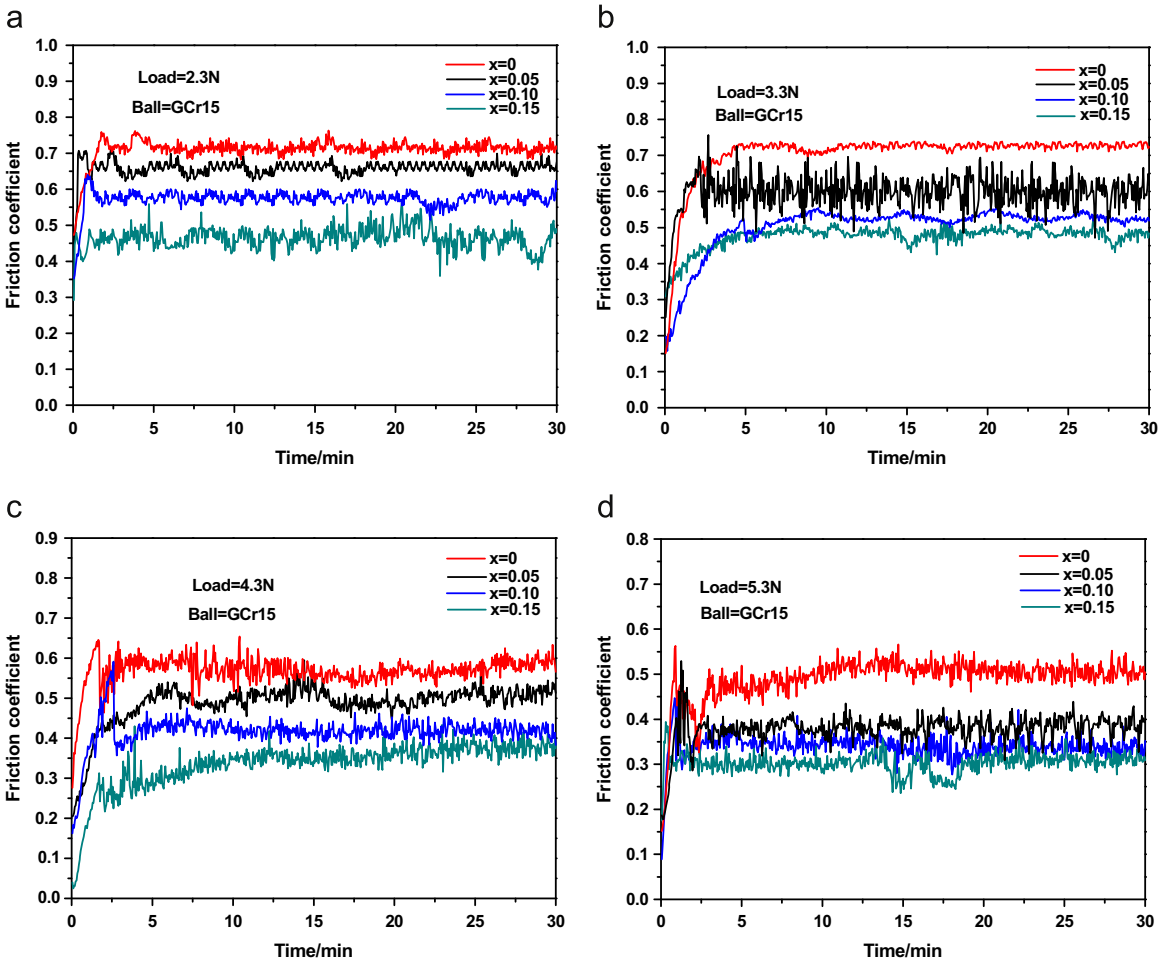

Fig. 5. Coefficient of friction against sliding times for the $(Mo_{1-x}Cr_x)Si_2$ films sliding against GCr15 bearing steel ball under normal loads of 2.3, 3.3, 4.3 and 5.3 N.

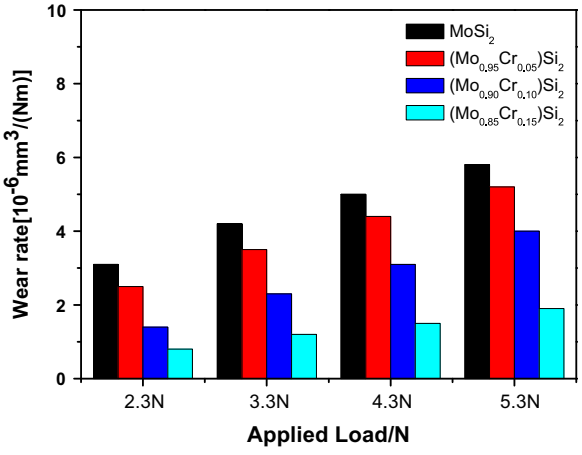

Fig. 6. Variation of specific wear rates for the four $(Mo_{1-x}Cr_x)Si_2$ films as a function of applied normal load after a sliding distance of 396 m at room temperature.

$MoSi_2$ film) in the tribochemical layer is derived from a material transfer from GCr15 steel counterpart onto worn surface of the films. Compared with the $MoSi_2$ film, a lower concentration of Fe was detected from the worn surface of the $(Mo_{0.85}Cr_{0.15})Si_2$ film, indicating that the counterpart GCr15 steel ball undergoes milder wear damage than that sliding against the $MoSi_2$ film. Because these mixed oxides can act as solid lubricants, such as MoO_3 [27,28], lowering the tangential forces and preventing adhesive contact between the films and counterpart GCr15 steel balls, the mechanical properties and bond strength of tribo-oxidation oxide layers plays a significant role in controlling the wear damage of the as-deposited films. As evidenced by morphological observations, the tribo-oxidation oxide layer produced on wear track of the $MoSi_2$ film is poorly protective with microcracks and spallation, and is easily removed by plowing action of hard asperities on the counterpart GCr15 steel ball. It is thereby susceptible to oxidative wear caused by repetitive disruption of oxide films. In contrast, it seems that with increasing Cr addition, the tribochemical layers formed on wear track of the three Cr-containing $MoSi_2$ films show more compact, continuous and uniform surface morphologies, thus weakening the scratching effect and reducing the wear rates. In addition, higher hardness of the three Cr-containing $MoSi_2$ films provides enough supporting for the soft tribo-oxidation surface layer, and this negative hardness-gradient is a desirable surface characteristic to achieve a low wear rate [27].

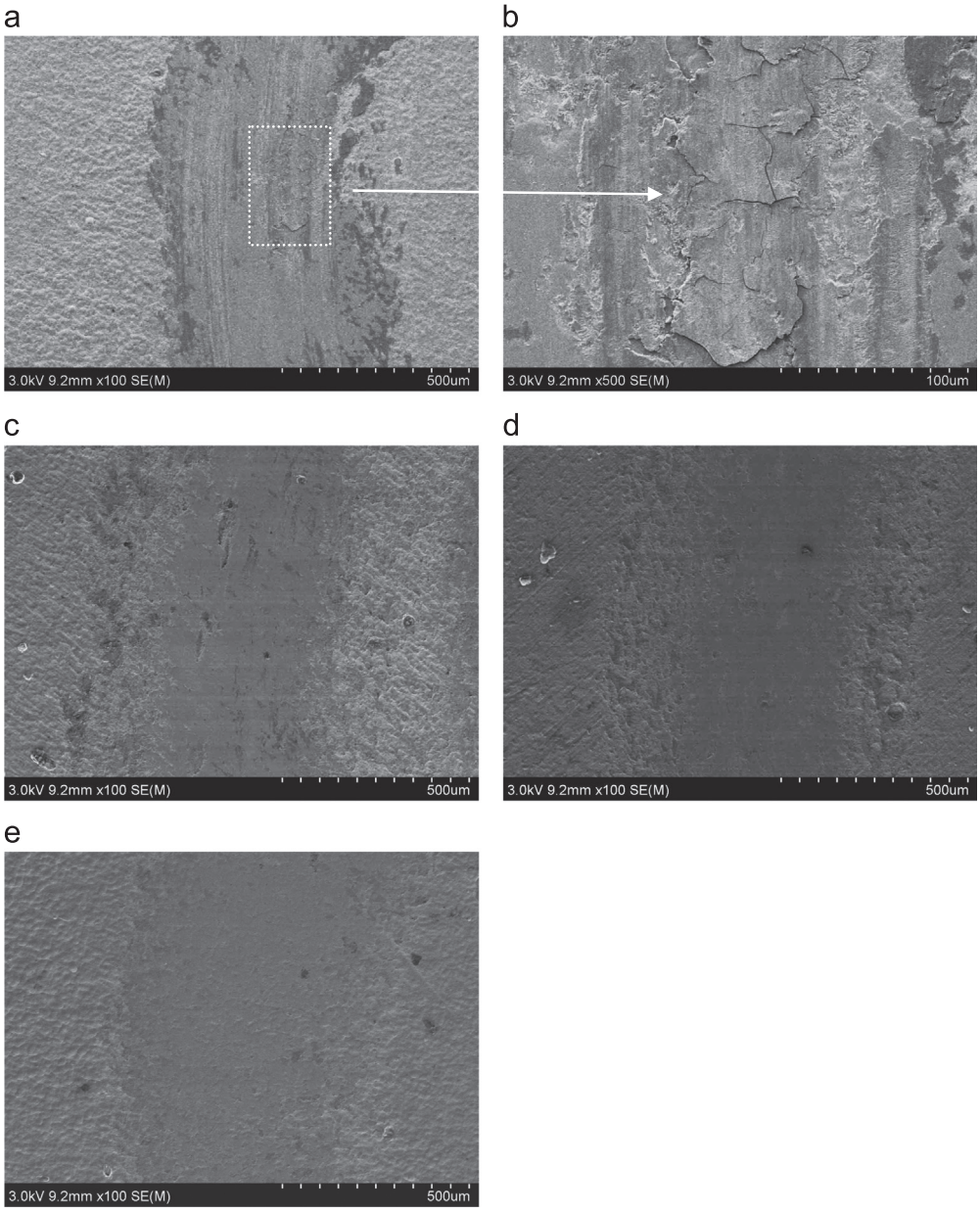

Fig. 7. SEM images of the worn surface morphologies of the four $(Mo_{1-x}Cr_x)Si_2$ films sliding against GCr15 steel balls under a normal load of 5.3 N. (a) $MoSi_2$, (b) higher magnification image of a selected area in (a), (c) $(Mo_{0.95}Cr_{0.05})Si_2$, (d) $(Mo_{0.90}Cr_{0.10})Si_2$, and (e) $(Mo_{0.85}Cr_{0.15})Si_2$.

3.4. Low-temperature cyclic oxidation behavior

3.4.1. Cyclic-oxidation kinetics

Fig. 9 shows the kinetic curves of cyclic oxidation of the four $(Mo_{1-x}Cr_x)Si_2$ films at 500 °C in air. For all the tested specimens, no oxide scales spallation occurred during thermal cycling up to 100 cycles. It is obvious that the weight gains of the films increase with the increase of the oxidation time, and at the same oxidation time, the weight gains significantly decease with increasing Cr content, indicating the positive influence of Cr alloying on the oxidation resistance of the $MoSi_2$ films.

Examination of the oxidation kinetics indicates a small deviation from parabolic behavior for the four films. The curves show that for all four films the oxidation process can be described by a power type law of the form [28]:

$$\frac{\Delta w}{S} = K_m t^m \tag{1}$$

where $\Delta W/S$ is the weight gain per unit surface area of the sample after an exposure of time, t, whilst K_m and m are the power law rate constant and the rate exponent, respectively. Table 1 gives the kinetics parameters of the four $(Mo_{1-x}Cr_x)Si_2$ films oxidized at 500 °C in air (R is the correlation coefficient in Table 1). As can be seen, the values of the rate exponent m are around 0.5, denoting that the oxidation kinetics of the four $(Mo_{1-x}Cr_x)Si_2$ films follow a subparabolic rate law over the entire exposure time. With the increase of Cr content,

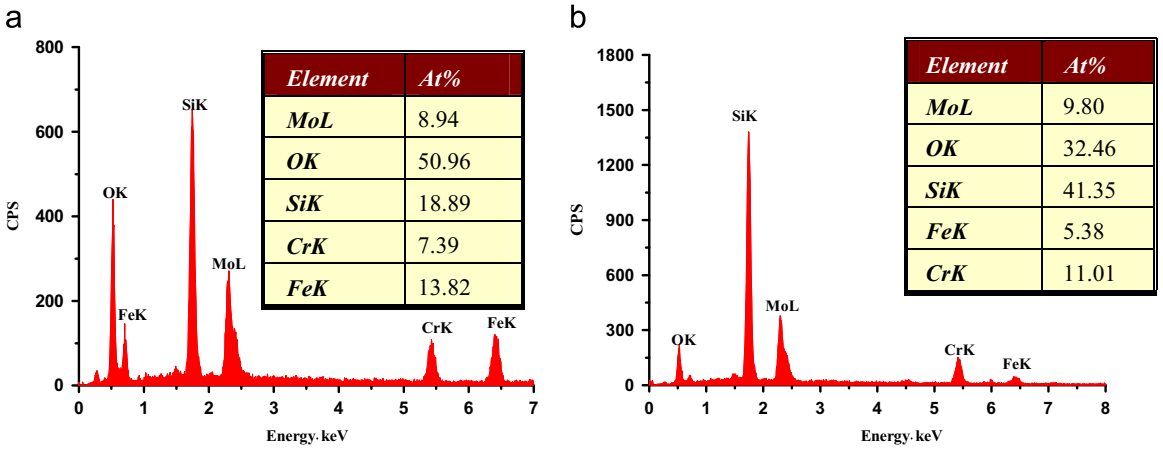

Fig. 8. EDS area analysis from the worn tracks on (a) the $MoSi_2$ film and (b) the $(Mo_{0.85}Cr_{0.15})Si_2$ film.

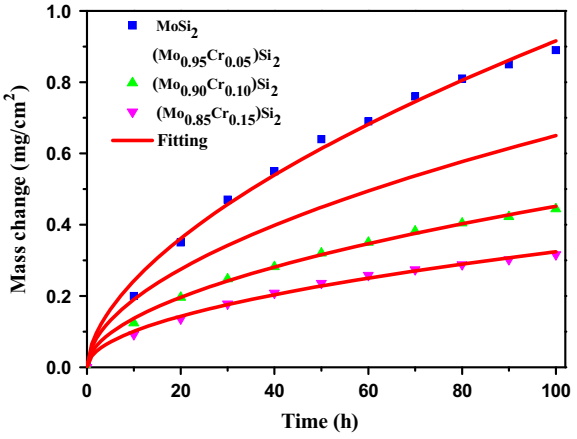

Fig. 9. Mass change as a function of exposure time for the $(Mo_{1-x}Cr_x)Si_2$ films exposed at 500 °C in air.

the values of m and K_m decrease accordingly, implying that Cr additions reduce the oxidation rates of the $(Mo_{1-x}Cr_x)Si_2$ films.

3.4.2. Characterization of the oxidation product

To determine the reasons for the observed improvement of the oxidation resistance of the $(Mo_{1-x}Cr_x)Si_2$ films by Cr alloying, the chemical compositions, oxidation products and the surface morphologies of oxide scales were examined. Fig. 10 shows the XRD patterns of the four $(Mo_{1-x}Cr_x)Si_2$ films after cyclic-oxidation tests for 20 h at 500 °C. The X-ray patterns of the oxide scales formed on the films reveal that the diffraction peaks for the underlying C40-$(Mo_{1-x}Cr_x)Si_2$ film are clearly visible for all samples. This means that the incident X-rays penetrated the oxide layer presumably because the oxide scales are very thin. Weak peaks of MoO_3 were identified for the monolithic binary $MoSi_2$ film. Meanwhile diffraction peaks for both Cr_2O_3 and $Cr_2(MoO_4)_3$ were detected for the three Cr-containing $(Mo_{1-x}Cr_x)Si_2$ films. The intensity of peaks for these phases gradually increased with Cr additions, which is in accordance with the data reported by Ström et al. [14]. No diffraction lines for crystalline SiO_2 were evident in the XRD patterns, confirming that silica formed is presumably present in amorphous form.

Table 1
Summary of rate constants processed from the oxidation data.

Materials	k_m	m	R
$MoSi_2$	0.0085	0.577	0.9945
$(Mo_{0.9}Cr_{0.1})Si_2$	0.0045	0.534	0.9921
$(Mo_{0.8}Cr_{0.2})Si_2$	0.0021	0.514	0.9918
$(Mo_{0.7}Cr_{0.3})Si_2$	0.0011	0.498	0.9958

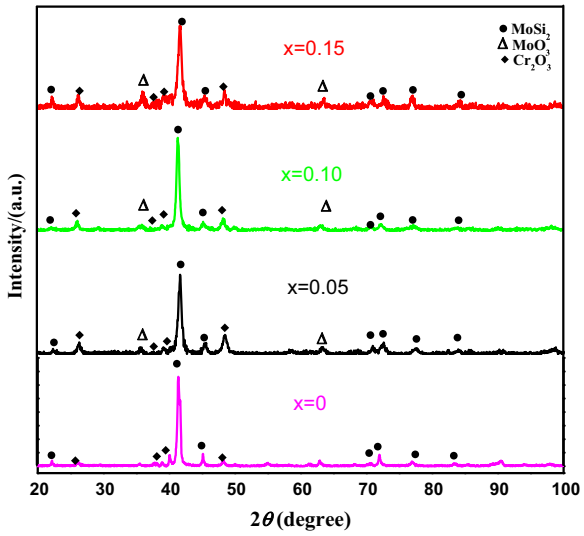

Fig. 10. X-ray diffraction patterns recorded from the four $(Mo_{1-x}Cr_x)Si_2$ films after cyclic-oxidation for 20 h at 500 °C.

3.4.3. Surface morphologies of oxide scales

Figs. 11–13 show the typical surface oxides morphologies formed on the four $(Mo_{1-x}Cr_x)Si_2$ films oxidized at 500 °C for different times. SEM examination of the scale surface reveals that after10 h of oxidation, some regions of the oxide scale surface for the monolithic $MoSi_2$ film are decorated with small

and thin platelet-like crystals projecting outward from the oxide scale, as can be seen in Fig. 11(a) and (b). EDS area analysis reveals that the platelet-like oxides mainly contained Mo and O with a ratio of Mo to O of approximately 1:3, consistent with the presence of MoO_3 (Fig. 11(c)); whereas the remaining scales exhibited a Si/Mo atomic ratio close to that of $MoSi_2$ (Fig. 11(d)), implying that MoO_3 and SiO_2 are found to form simultaneously. By comparison, the dense and continuous oxide scales are formed on the surface of Cr-alloyed $MoSi_2$ films, as shown in Fig. 11(e)–(g)). EDS area analysis shows that Cr additions can effectively promote the enrichment of Si and increase the Si/Mo atomic ratios in the oxide scales (Fig. 11(h)–(j)), in other words, Cr addition facilitate selective oxidation of Si for the three Cr-containing $MoSi_2$ films. With extended exposure time (20 h), the oxide scale on the monolithic $MoSi_2$ film covers with some micro-cracks, and the size and density of these platelet-like MoO_3 increase significantly (Fig. 12(a)). As shown in Fig. 12(b), the oxide scale on the $(Mo_{0.95}Cr_{0.05})Si_2$ film exhibits a scaly morphology with a number of micro-pores. Nevertheless, the oxide scales on the $(Mo_{1-x}Cr_x)Si_2$ (x=0.10 and 0.15) films still remains dense and uniform surface morphologies (Fig. 12(c) and (d)), showing no evidence of defects and cracks. After a prolonged oxidation time up to 100 h (Fig. 13(a)), the oxide scale on the monolithic $MoSi_2$ film is porous and contains many large cracks, indicating that the monolithic $MoSi_2$ film has undergone severe oxidation. It is also noted that these large MoO_3 crystals are no longer visible on the oxide scale, suggesting that the rate of MoO_3 formation is lower than the evaporation rate with prolonged exposure [29]. For the $(Mo_{0.95}Cr_{0.05})Si_2$ film, the scale surface becomes more rough and the number of defects, such as micro-cracks and pores, increase noticeably, while the oxide scales on the $(Mo_{1-x}Cr_x)Si_2$ (x= 0.10 and 0.15) films still exhibit a relatively compact structure, except for some pinholes distributed between the scaly oxides.

3.4.4. *Characterization of oxide scales by impedance spectroscopy*

The above oxidation behavior measurements, such as weight change data and complementary electron microscope studies, employed to evaluate the growth rate and the evolution of oxide scale morphologies, still leave deficiencies in understanding. For example, because of the weight loss due to volatilization of MoO_3 during oxidation, simple weight change measurement is always ambiguous. Moreover, it is difficult to use electron microscopy to examine defects, such as pores, channels, or cracks that may be present inside the oxide scale by surface morphology observation, whilst cross-sectional morphology observations are normally restricted to localized areas or require destructive preparation methods. Electrochemical-impedance

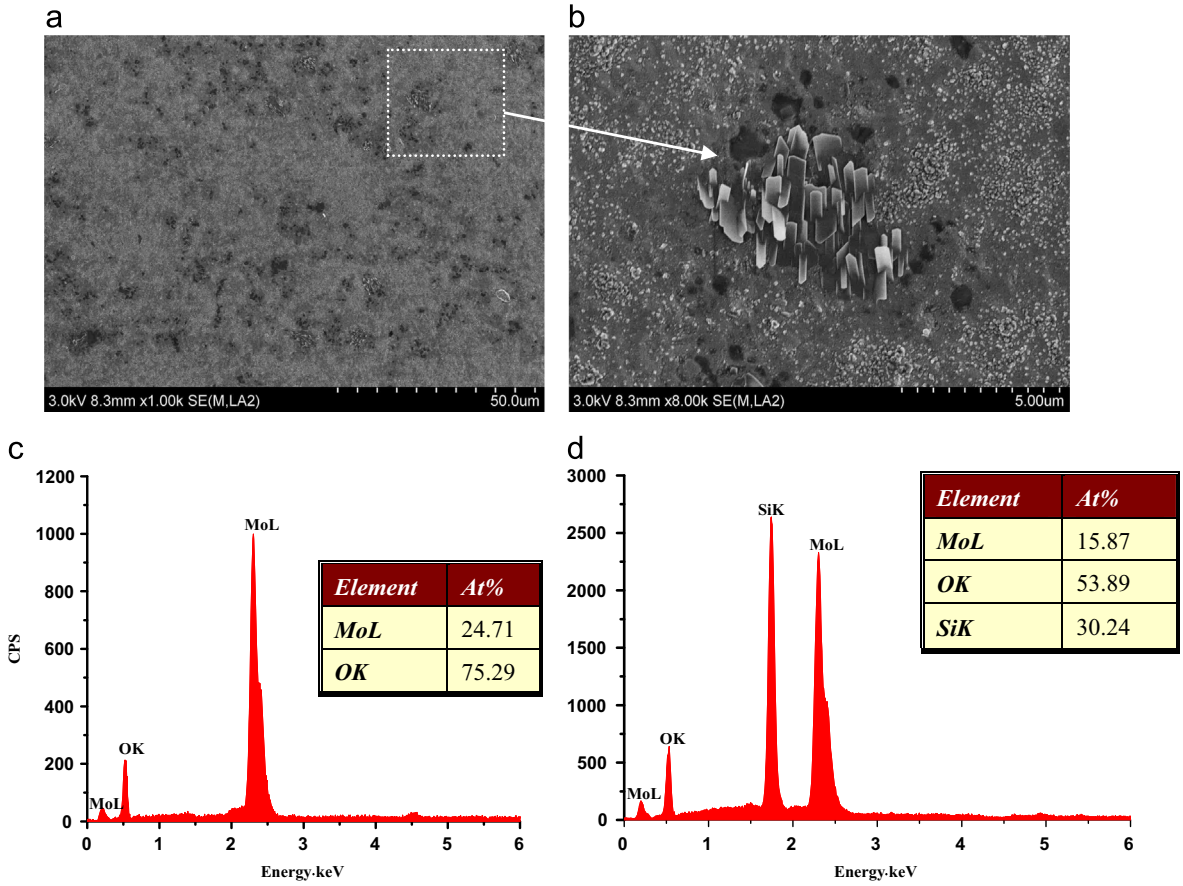

Fig. 11. SEM micrographs of surface morphologies and EDX analyses of oxide scales on the four $(Mo_{1-x}Cr_x)Si_2$ films oxidized at 500 °C for 10 h. (a) $MoSi_2$ film; (b) high magnification image of a selected area in (a); EDS area analysis of (c) platelet-like crystals and (d) the remaining scales; (e) $(Mo_{0.95}Cr_{0.05})Si_2$, (f) $(Mo_{0.90}Cr_{0.10})Si_2$, (g) $(Mo_{0.85}Cr_{0.15})Si_2$, EDS area analysis of the oxide scales on (h) $(Mo_{0.95}Cr_{0.05})Si_2$, (i) $(Mo_{0.90}Cr_{0.10})Si_2$ and (j) $(Mo_{0.85}Cr_{0.15})Si_2$.

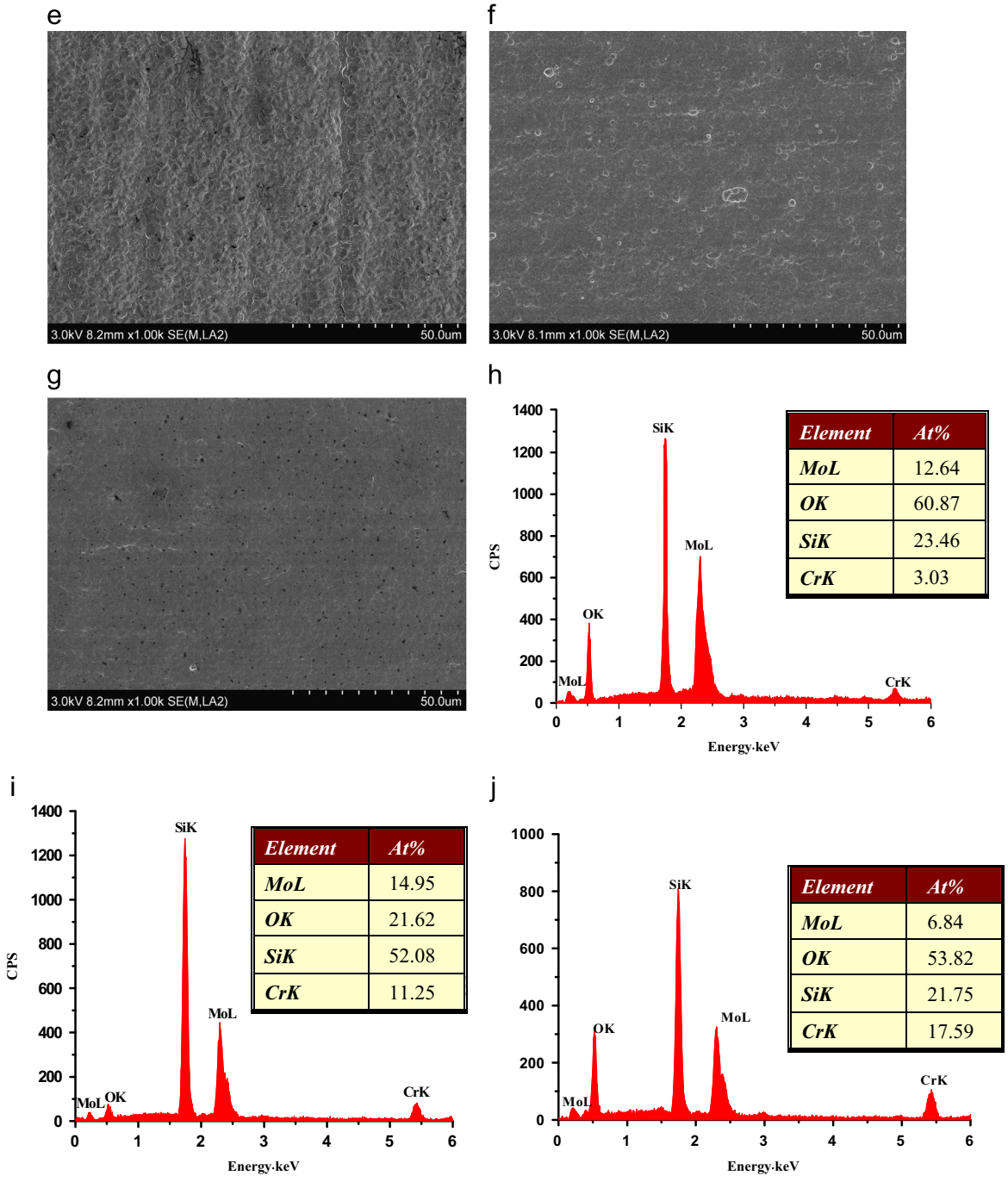

Fig. 11. (*continued*)

spectroscopy (EIS) is an effective tool for characterizing the structural features of different types of surface oxide scales on metal and alloys substrates, particularly to determine the compact/porous nature of a film. Therefore, to gain a deeper insight into the influence of Cr alloying on the oxidation resistance of $MoSi_2$, the electrochemical behavior of the films oxidized for various times at 500 °C was investigated in a 3.5 wt% NaCl solution by EIS.

Fig. 14 shows the Nyquist and Bode plots of the $(Mo_{1-x}Cr_x)Si_2$ films oxidized at 500 °C for 10 h at respective OCP in a 3.5 wt% NaCl solution. The symbols represent the experimental data and the solid lines represent the simulated data, generated using the equivalent circuit in Fig. 15. It is clear that the Nyquist plots for the $(Mo_{1-x}Cr_x)Si_2$ films show only a capacitance-like semicircle which presents one reaction time constant. It is evident that the diameter of the semicircles increases with increasing Cr content in the four films. The frequency response of the oxide scales on the $(Mo_{1-x}Cr_x)Si_2$ ($x=0.10$ and 0.15) films shows a more pronounced capacitive behavior, due to the fact that only a minor part of the large semi-circle corresponding the oxide scales is measurable over the frequency range used. As shown in Fig. 14(b), the

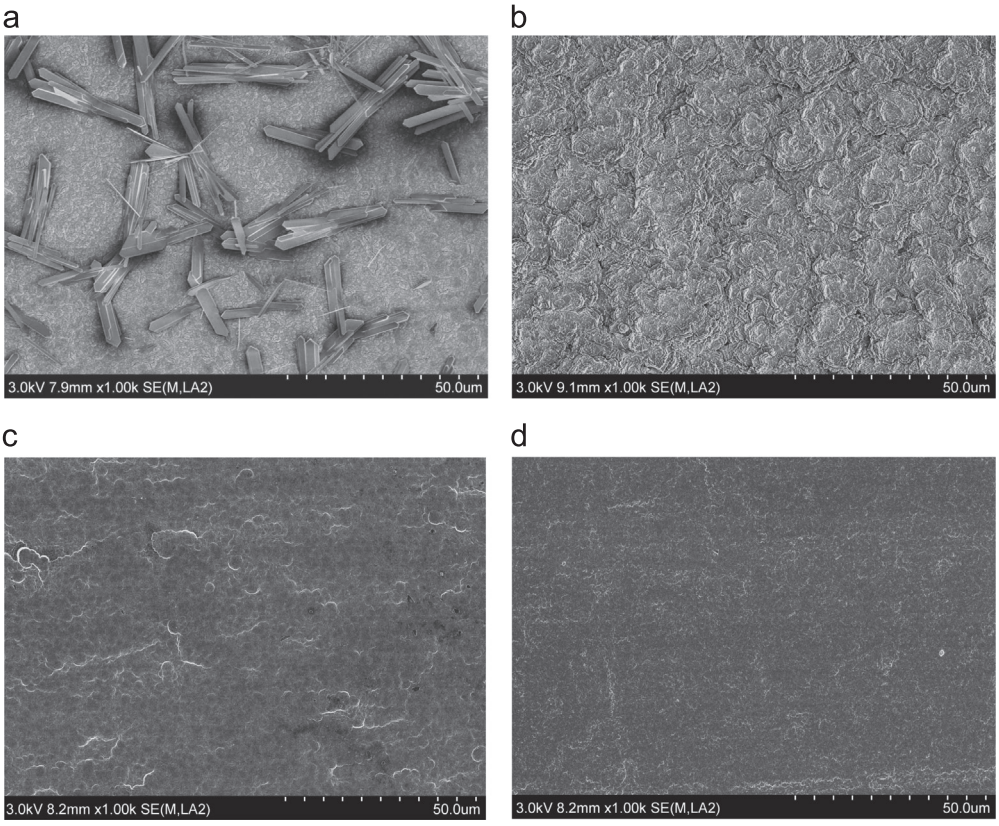

Fig. 12. SEM micrographs of surface morphologies of the four $(Mo_{1-x}Cr_x)Si_2$ films oxidized at 500 °C for 20 h. (a) $MoSi_2$, (b) $(Mo_{0.95}Cr_{0.05})Si_2$, (c) $(Mo_{0.90}Cr_{0.10})Si_2$, and (d) $(Mo_{0.85}Cr_{0.15})Si_2$.

corresponding Bode plots consist of three distinctive segments that depend on the frequency range. In the high frequency region, the log |Z| versus log f plots (Bode magnitude plot) are virtually independent of frequency, with the phase angle value approaching 0°. This is a typical response for a resistive behavior and corresponds to the resistance of the saline solution between the working and the reference electrode. In the medium frequency region, a linear relationship can be observed between the log |Z| and the log f with a slope close to −1 and phase angle approximately −90°. These features are characteristic of a purely capacitive behavior at the electrode/electrolyte interface, suggesting that the protective oxide scales, acting as diffusion barrier between the films and the oxidizing environment, have formed on the four $(Mo_{1-x}Cr_x)Si_2$ films. In the low-frequency region, resistive behavior of the electrode is not evident; this is, a region where the absolute impedance is independent of the frequency is not attained. The experimental impedance data of the $(Mo_{1-x}Cr_x)Si_2$ films oxidized at 500 °C for 10 h were fitted to an equivalent circuit known as Randles circuit shown in Fig. 15. The physical significance of the circuit elements is as follows: R_s is the solution resistance, and Q_p and R_p are representations of the capacitive and the resistive behavior of the oxide scales. As shown in Fig. 14, the fitted and measured results match very well with each other, suggesting the validity of the proposed circuit model. For the sake of fitting quality, all the capacitors were taken as Constant Phase Elements (CPE or Q), whose impedance is given by $Z_{CPE}=[Q(jw)^n]^{-1}$, where Q is the CPE coefficient, j is the imaginary unit and ω is the angular frequency. The value of n gives information on the nature of the CPE, being $n=1$ for a pure capacitor and $n\sim0.5$ for a mass transfer process. Inspection of the data of Table 2 reveals that the R_p values are observed to increase with the addition of Cr into $MoSi_2$. Moreover, the values of the CPE exponent n for all $(Mo_{1-x}Cr_x)Si_2$ films are very close to unity ($n>0.92$), indicating that the oxide scales that act with near capacitive behavior are very homogenous and compact.

Fig. 16 displays the Nyquist and Bode plots for the $(Mo_{1-x}Cr_x)Si_2$ films oxidized at 500 °C for 20 h at respective OCP in a 3.5 wt% NaCl solution. Compared with the EIS spectra shown in Fig. 14, the recorded EIS spectra for the films after 20 h of oxidation show a more depressed capacitive loop in the Nyquist plot, and narrower phase plateaus in the medium frequency region and a smaller absolute impedance modulus at low frequency |Z|, indicating a less capacitive response and a reduction in corrosion resistance in the electrolytes used for these oxide scales [30–32]. As shown in Fig. 16(a), a new incomplete capacitive loop appears in the low frequency region in the Nyquist plots for the $(Mo_{1-x}Cr_x)Si_2$ ($x=0$ and 0.05) films, reflecting the presence of two time constants in the normal frequency range. The results indicate that the oxide scales on the $(Mo_{1-x}Cr_x)Si_2$ ($x=0$ and 0.05) films exhibit a two-layer structure, consisting of a compact inner layer and a porous outer layer. Based on the experimental evidence, the

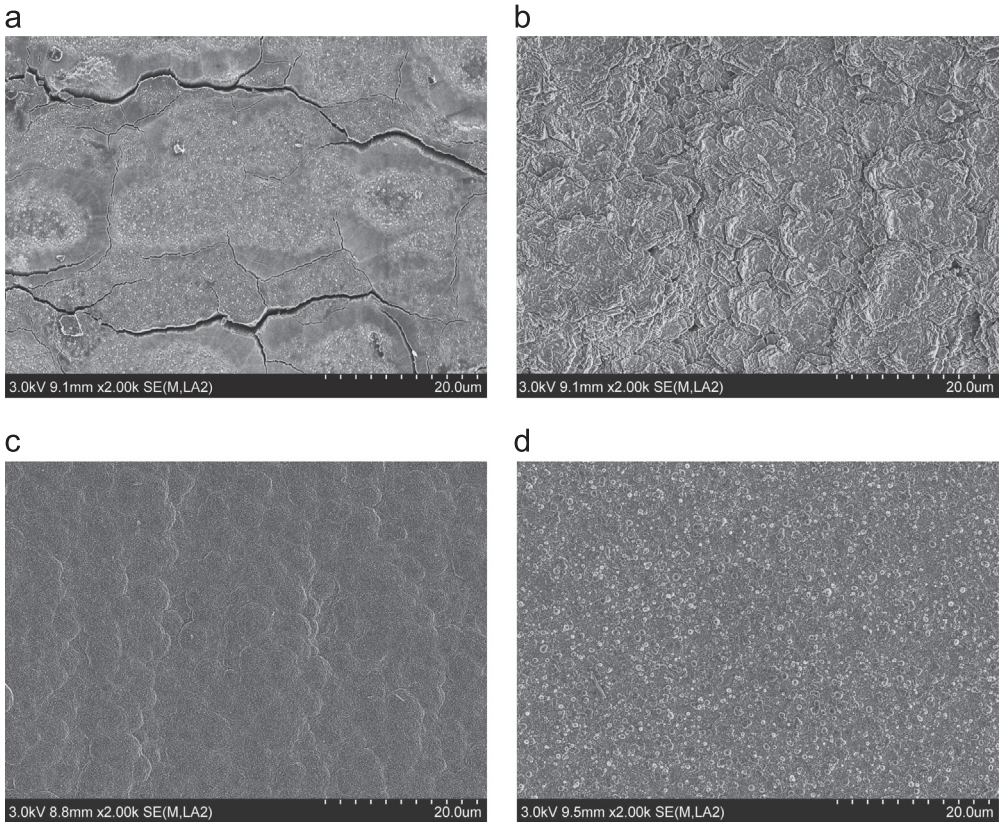

Fig. 13. SEM micrographs of surface morphologies of the four $(Mo_{1-x}Cr_x)Si_2$ films oxidized at 500 °C for 100 h. (a) $MoSi_2$, (b) $(Mo_{0.95}Cr_{0.05})Si_2$, (c) $(Mo_{0.90}Cr_{0.10})Si_2$, and (d) $(Mo_{0.85}Cr_{0.15})Si_2$.

experimental EIS data of the $(Mo_{1-x}Cr_x)Si_2$ ($x=0$ and 0.05) films are interpreted by an electrical equivalent circuit composed of two capacitive/resistive elements in series, as shown in Fig. 17. The CPE_p-R_p is corresponding to the high frequency and the CPE_b-R_b to the low frequency loops. In this case, the overall resistance of oxide scales, R_t, was calculated as the sum of R_b and R_p. This circuit has been previously described elsewhere [33–35]. For the $(Mo_{1-x}Cr_x)Si_2$ (x=0.10 and 0.15) films, the impedance data are fitted using a simple R_s (QR_p) circuit shown as in Fig. 15. The fitting parameters of the circuit elements are given in Table 3. For the $(Mo_{1-x}Cr_x)Si_2$ ($x=0$ and 0.05) films with a double-layer structured oxide scale, the resistances values for the inner barrier layer (R_b) are larger than that for the outer, more porous, layer (R_p), revealing that the inner barrier layer is predominantly responsible for their anticorrosive protection. The overall resistance of the oxide scales on the four films (R_p for $x=0.10$ and 0.15; R_t for $x=0$ and 0.05) still increases with Cr content in the films. Fig. 18 shows the Nyquist and Bode plots for the $(Mo_{1-x}Cr_x)Si_2$ films oxidized at 500 °C for 100 h at respective OCP in a 3.5 wt% NaCl solution. The Nyquist plots of the four films present two distinguished capacitive semi-circles, corresponding to two clear phase angle peaks located in the high and low frequency ranges observable in the Bode phase plots. In comparison with the impedance response shown in Fig. 16(a), the radius of the measured capacitive semi-circle for the four films is further reduced, which means that the barrier ability of the oxide scales formed on the films has become weaker with prolonging exposure time. Such impedance spectra are fitted using the equivalent circuit shown in Fig. 17 and the values of R_p and R_b derived from the fitting of the experimental impedance data are present in Table 4. It is clear that the values of R_p and R_b for the oxide scales formed after 100 h of oxidation are about one order of magnitude lower than that for the oxide scales formed after 20 h of oxidation. This suggests that the increase in oxidation time leads not only to a noticeable increase in defect level of the outer layer, but also defects extending into the inner barrier layer. Therefore, the oxide scales become more defective after 100 h of oxidation, which is also corroborated by SEM observation of surface morphologies of the oxide scales.

It is generally accepted that the porous and non-protective oxide scale formed on the monolithic $MoSi_2$ at low temperature is due to the volume expansion derived from the simultaneous oxidation of molybdenum and silicon, and the most probable evaporation of molybdenum species $(MoO_3)_3$ escaped from the surface of the oxide scale that prevents the formation of a continuous silica scale [36]. Similarly, in the current work, as evidenced by EDX analysis, for the monolithic $MoSi_2$ film, its oxide scale conserves the initial Mo/Si ratio characteristic of the stoichiometric value for $MoSi_2$, and significant volume expansion caused by the non-selective oxidation generates a large internal stress. During the initial stage of oxidation, the scale on the monolithic $MoSi_2$ film

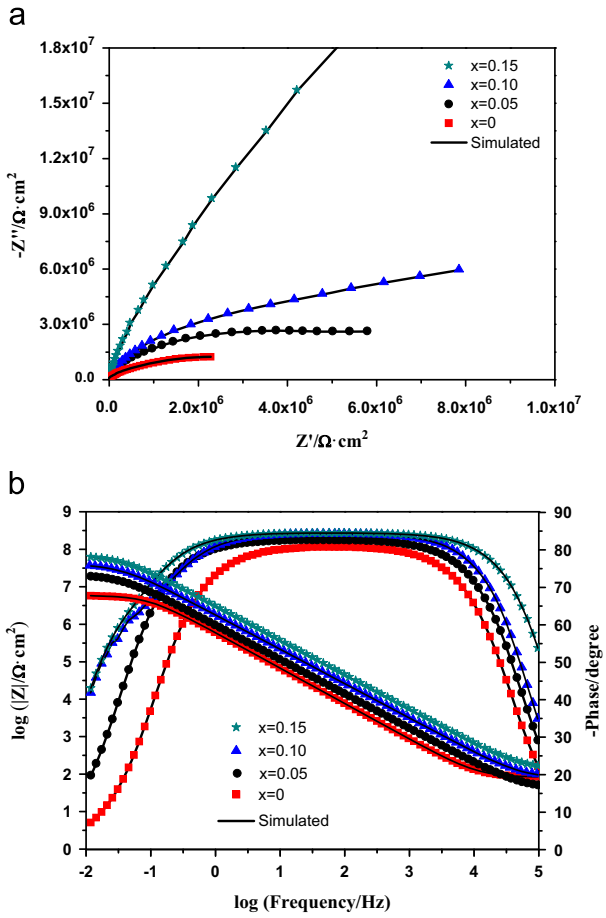

Fig. 14. (a) Nyquist and (b) Bode plots for the $(Mo_{1-x}Cr_x)Si_2$ films oxidized at 500 °C for 10 h at respective OCP in a 3.5 wt% NaCl solution. Symbols are experimental data and solid lines are fitted results.

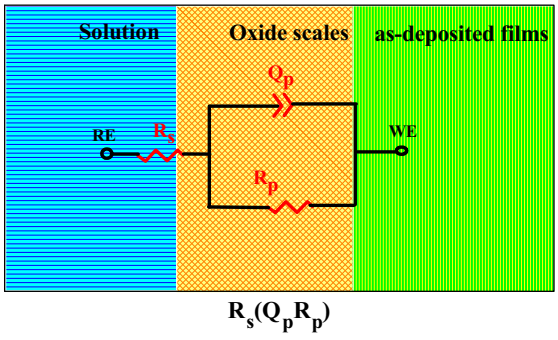

Fig. 15. Electronic equivalent circuit used to fit the impedance data of the $(Mo_{1-x}Cr_x)Si_2$ films oxidized at 500 °C for 10 h.

Table 2
Equivalent electrical circuit parameters for the $(Mo_{1-x}Cr_x)Si_2$ films after being oxidized at 500 °C for 10 h.

Samples	R_s (Ω cm^2)	Q_p (Ω^{-1} cm^{-2} s^n)	n	R_p (Ω cm^2)
$MoSi_2$	18.23	2.90E−7	0.902	2.25E6
$(Mo_{0.9}Cr_{0.1})Si_2$	20.34	3.38E−7	0.918	5.87E6
$(Mo_{0.8}Cr_{0.2})Si_2$	21.32	3.96E−7	0.941	1.04E7
$(Mo_{0.7}Cr_{0.3})Si_2$	23.98	5.91E−7	0.948	8.76E7

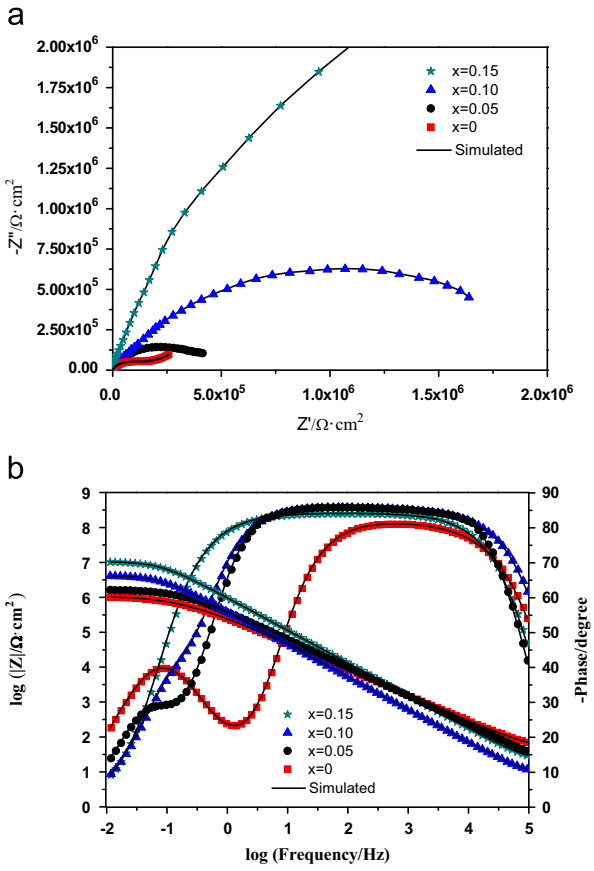

Fig. 16. (a) Nyquist and (b) Bode plots for the $(Mo_{1-x}Cr_x)Si_2$ films oxidized at 500 °C for 20 h at respective OCP in a 3.5 wt% NaCl solution.

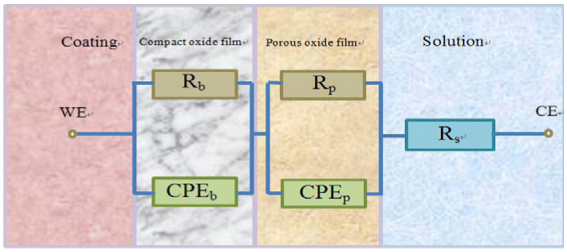

Fig. 17. Electronic equivalent circuit used to fit the impedance data of the $(Mo_{1-x}Cr_x)Si_2$ films oxidized at 500 °C for 20 h (for both $x=0$ and 0.05) and 100 h.

exhibits protective behavior because the stress has not accumulated sufficiently to introduce cracks and defects. The outward growth of platelet-like MoO_3 requires the outward diffusion of molybdenum cation, which is counterbalanced by an inward flux of vacancies, and the subsequent coalescence of excess vacancies may give rise to void formation at the scale–metal interface [37]. With extended exposure time, it can be observed that the pre-existing micro-cracks are broadened by a local wedging effect, aggravating further the severity of oxidation damage. Moreover, the formation of volatile MoO_3 leads to the oxide scale with a porous structure that promotes oxygen transport through the oxide scale along these lower-energy paths, accelerating the oxidation process [5]. In contrast, as confirmed by the kinetic curves of cyclic oxidation

Table 3
Equivalent electrical circuit parameters for the $(Mo_{1-x}Cr_x)Si_2$ films after being oxidized at 500 °C for 20 h.

Samples	R_s (Ω cm^2)	CPE$_p$		R_p (Ω cm^2)	CPE$_b$		R_b (Ω cm^2)
		$Y_{0\text{-}p}$ (Ω^{-1} cm^{-2} s^n)	n_p		$Y_{0\text{-}b}$ (Ω^{-1} cm^{-2} s^n)	n_p	
$MoSi_2$	9.87	4.288E−6	0.744	2.16E6	2.706E−6	0.821	4.32E6
$(Mo_{0.9}Cr_{0.1})Si_2$	10.10	2.134E−6	0.773	2.59E6	1.579E−7	0.878	6.25E6
$(Mo_{0.8}Cr_{0.2})Si_2$	13.23	1.956E−7	0.835	1.05E7	/	/	/
$(Mo_{0.7}Cr_{0.3})Si_2$	21.14	1.868E−7	0.862	1.48E7	/	/	/

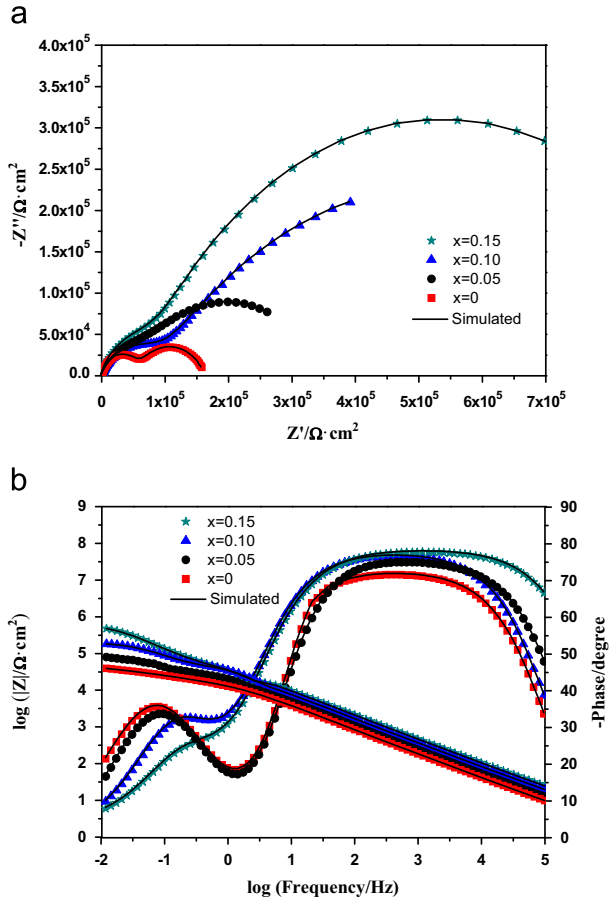

Fig. 18. (a) Nyquist and (b) Bode plots for the $(Mo_{1-x}Cr_x)Si_2$ films oxidized at 500 °C for 100 h at respective OCP in a 3.5 wt% NaCl solution.

and the surface morphologies observation, with increasing Cr content, the oxide scales formed on the surface of the three Cr-containing $MoSi_2$ films become smoother and denser with fewer defects, which can act as diffusion barrier for the diffusion of anions and cations manifested by lower oxidation rate constants. Minimization of the crack formation in the oxide scale through the suppressing of the growth of massive MoO_3 precipitates and its volatilization is prerequisite to impede the accelerated oxidation of $MoSi_2$ [12]. As described above, Cr alloying has beneficial effect on oxidation behavior of $MoSi_2$ manifested by facilitating selective oxidation of Si and reducing the amount of Mo oxide in the scales accordingly.

Westbrook et al. [8] proposed that the catastrophic nature of the pest oxidation was attributed to the fact that oxygen can diffuse rapidly through the sample along grain boundary paths, and subsequently grain boundary embrittlement occurs. However, other studies indicated that grain boundary itself does not provide a sharp tip needed for a crack initiation and is not the dominant site for pest oxidation [38]. Zhang et al. [39] attempted to identify the individual contributions from porosity, cracking and grain boundaries on pest oxidation [39]. They compared the pest behaviors of as-cast, spark plasma sintered poly-crystalline $MoSi_2$ and $MoSi_2$ single crystal at 500 °C. Their results showed that grain boundary does affect the oxidation resistances of dense poly-crystal and single crystal materials. The oxidation kinetics changes from non-protective linear law for the poly-crystal material to protective parabolic law for the $MoSi_2$ single crystal. If the pest oxidation prefers to take place at grain boundaries, the four $(Mo_{1-x}Cr_x)Si_2$ nanocrystalline films in the present study should be more prone to pest disintegration than the coarser grained $MoSi_2$. However, there is no evidence that the grain boundary was the main reason for pesting as compared to the experimental observation described in the literature. For example, Knittel et al. [40] found that coarse grained $MoSi_2$ specimens synthesized by arc melting disintegrated into powder after oxidation for 17 h at 500 °C. In fact, it has been extensively reported that the oxide scales formed on nanocrystalline materials exhibit improved resistance to cracking and spallation [41,42]. Further, the oxides formed on nano-crystalline materials were pegged onto the grain boundaries to form a convoluted interface, known as"micro-pegging" effect, leading to better scale adhesion to the substrate[43].

4. Conclusions

Four types of nanocrystalline $(Mo_{1-x}Cr_x)Si_2$ films with differing Cr contents are prepared onto Ti–6Al–4V substrates by using a double cathode glow discharge apparatus. The hardness and elastic modulus of the four $(Mo_{1-x}Cr_x)Si_2$ films monotonically increase with increasing Cr content in the films, suggesting that alloying C40-structured $MoSi_2$ with Cr results in solid solution hardening. When the normal loads vary from 2.3 N to 5.3 N, the specific wear rates of the $(Mo_{1-x}Cr_x)Si_2$ films are in the order of 10^{-6} mm^3/(N m), and decrease with increasing Cr content. The oxidation behavior of the four $(Mo_{1-x}Cr_x)Si_2$ films obeys a subparabolic relation with the

Table 4
Equivalent electrical circuit parameters for the $(Mo_{1-x}Cr_x)Si_2$ films after being oxidized at 500 °C for 100 h.

Samples	R_s (Ω cm^2)	CPE_p		R_p (Ω cm^2)	CPE_b		R_b (Ω cm^2)
		$Y_{0\text{-}p}$ (Ω^{-1} cm^{-2} s^n)	n_p		$Y_{0\text{-}b}$ (Ω^{-1} cm^{-2} s^n)	n_b	
$MoSi_2$	13.24	2.75 E−5	0.621	9.01E4	1.95E−5	0.714	1.08E5
$(Mo_{0.9}Cr_{0.1})Si_2$	16.05	2.95 E−5	0.653	9.92E4	2.04E−6	0.733	1.58E5
$(Mo_{0.8}Cr_{0.2})Si_2$	17.04	4.28E−5	0.682	1.02E5	2.44E−6	0.781	1.83E5
$(Mo_{0.7}Cr_{0.3})Si_2$	22.61	5.72E−5	0.727	1.34E5	2.72E−6	0.792	1.85E5

overall exposure, and the cyclic oxidation rate of the films decreases with an increase in Cr content. The electrochemical behavior of the oxide scales immersed in a 3.5 wt% NaCl solution, following prior oxidation for various times at 500 °C, was evaluated by EIS measurements. The results show that with the increase of oxidation time, the oxide scales developed on the four films become defective, changing from a homogeneous and dense structure to a duplex structure consisting of a porous outer layer and a denser inner layer. The protective character of the oxide scales is strengthened with increases in Cr content in the films.

Acknowledgments

The authors acknowledge the financial support of the National Natural Science Foundation of China under Grant nos. 51175245 and 51374130 and the Aeronautics Science Foundation of China under Grant no. 2013ZE52058.

References

[1] T. Nakano, W. Azuma, Y. Umakoshi, Tensile deformation and fracture behaviour in $NbSi_2$ and $MoSi_2$ single crystals, Acta Mater. 50 (2002) 3731.
[2] H.A. Zhang, P. Chen, M.J. Wang, X.Y. Liu, Room-temperature mechanical properties of $WSi_2/MoSi_2$ composites, Rare Met. 21 (2002) 304.
[3] A.A. Sharif, A. Misra, T.E. Mitchell, Strength of $MoSi_2$-based crystals at ultra-high temperature, Scr. Mater. 52 (2005) 399.
[4] K. Yanagihara, T. Maruyama, K. Nagata, Effect of third elements on the pesting suppression of Mo–Si–X intermetallics (x = Al, Ta, Ti, Zr and Y), Intermetallics 4 (1996) 133.
[5] Y.Q. Liu, G. Shao, P. Tsakiropoulos, On the oxidation behaviour of $MoSi_2$, Intermetallics 9 (2001) 125.
[6] K. Hansson, M. Halvarsson, J.E. Tang, P. Pompe, M. Sundberg, J. E. Svensson, Oxidation behaviour of a $MoSi_2$-based composite in different atmospheres in the low temperature range (400–550 °C), J. Eur. Ceram. Soc. 24 (2004) 3559.
[7] D.A. Bertiss, R.R. Cerchiara, E.A. Gulbransen, F.S. Pettit, G.H. Meier, Oxidation of $MoSi_2$ and comparison with other silicide materials, Mater. Sci. Eng. 155 (1992) 165.
[8] J.H. Westbrook, D.L. Wood, PEST degradation in beryllides, silicides, aluminides, and related compounds, J. Nucl. Mater. 12 (1964) 208.
[9] C.G. Mckamey, P.F. Tortorelli, J.H. De Van, C.A. Carmichael, A study of pest oxidation in polycrystalline $MoSi_2$, J. Mater. Res. 7 (1992) 2747.
[10] S. Becker, A. Rahmel, M. Schutze, Oxidation of $TiSi_2$ and $MoSi_2$, Solid State Ion. 53 (1992) 280.
[11] X. Fei, Y. Niu, H. Ji, L. Huang, X. Zheng, Oxidation behavior of Al_2O_3 reinforced $MoSi_2$ composite coatings fabricated by vacuum plasma spraying, Ceram. Int. 36 (2010) 2235.
[12] J.K. Yoon, G.H. Kim, J.H. Han, I.J. Shon, J.M. Doh, K.T. Hong, Low-temperature cyclic oxidation behavior of $MoSi_2/Si_3N_4$ nanocomposite coating formed on Mo substrate at 773 K, Surf. Coat. Technol. 200 (2005) 2537.
[13] Y. Harada, Y. Murata, M. Morinaga, Solid solution softening and hardening in alloyed $MoSi_2$, Intermetallics 6 (1998) 529.
[14] E. Ström, Y. Cao, M.Y. Yao, Low temperature oxidation of Cr-alloyed $MoSi_2$, Trans. Nonferrous Met. Soc. 17 (2007) 1282 (T Nonferr Metal Soc).
[15] J. Pan, C. Leygraf, R.F.A. Jargelius-Pettersson, J. Lindén, Characterization of high-temperature oxide films on stainless steels by electrochemical-impedance spectroscopy, Oxid. Met. 50 (1998) 431.
[16] L. Klein, S. Virtanen, Corrosion properties of novel γ′–strengthened Co-base superalloys, Corros. Sci. 66 (2013) 233.
[17] H.M. Wang, F. Cao, L.X. Cai, H.B. Tang, R.L. Yu, L.Y. Zhang, Microstructure and tribological properties of laser clad Ti_2Ni_3Si/NiTi intermetallic coatings, Acta Mater. 51 (2003) 6319.
[18] P. Barberis, A. Frichet, Characterization of Zircaloy-4 oxide layers by impedance spectroscopy, J. Nucl. Mater. 273 (1999) 182.
[19] S.H. Song, P. Xiao, An impedance spectroscopy study of oxide films formed during high temperature oxidation of an austenitic stainless steel, J. Mater. Sci. 38 (2003) 499.
[20] P.Y. Guo, C.L. Zeng, Y Shao, Z.S. Qin, Characterization of high-temperature oxide films on dysprosium-doped Fe-20Cr alloys by electrochemical techniques, J. Rare Earth 30 (2012) 1150.
[21] J. Xu, Z.H. Xie, P. Munroe, Effect of Cr alloying on friction and wear of sputter-deposited nanocrystalline $(Mo_xCr_{1-x})_5Si_3$ films, Intermetallics 19 (2011) 1146.
[22] W.C. Oliver, G.M. Pharr, An improved technique for determining hardness and elastic-modulus using load and displacement sensing indentation experiments, J. Mater. Res. 7 (1992) 1564.
[23] J. Xu, Y. Wang, S.Y. Jiang, The effects of substitution of Cr for Mo on the mechanical properties of nanocrystalline Mo_5Si_3 films, Nanoscale 2 (2010) 394.
[24] A.A. Sharif, A. Misra, J.J. Petrovic, T.E. Mitchell, Alloying of $MoSi_2$ for improved mechanical properties, Intermetallics 9 (2001) 869.
[25] H. Inui, K. Ishikawa, M. Yamaguchi, Effects of alloying elements on plastic deformation of single crystals of $MoSi_2$, Intermetallics 8 (2000) 1131.
[26] J. Xu, J.D. Wu, D.H. Lai, Z.H. Xie, P. Munroe, Investigation on effect of alloying elements on mechanical properties of $MoSi_2$ by first principle calculation, Mater. Sci. Technol. 28 (2012) 1337.
[27] Q. Yang, L.R. Zhao, P.C. Patnaik, X.T. Zeng, Wear resistant TiMoN coatings deposited by magnetron sputtering, Wear 261 (2006) 119.
[28] M.C. García-Alonso, J.L. González-Carrasco, M.L. Escudero, J. Chao, Oxidation behavior of fine-grain MA 956 superalloy, Oxid. Met. 53 (2000) 77.
[29] L. Ingemarsson, M. Halvarsson, J. Engkvist, T. Jonsson, K. Hellström, L. G. Johansson, J.E. Svensson, Oxidation behavior of a $Mo(Si, Al)_2$-based composite at 300–1000 °C, Intermetallics 18 (2010) 633.
[30] A. Amirudin, D. Thierry, Application of electrochemical impedance spectroscopy to study the degradation of polymer-coated metals, Prog. Org. Coat. 26 (1995) 1.
[31] A.I. Muñoz, J.G. Antón, J.L. Guiñón, V.P. Herranz, Inhibition effect of chromate on the passivation and pitting corrosion of a duplex stainless

steel in LiBr solutions using electrochemical techniques, Corros. Sci. 49 (2007) 3200.
[32] Z. Grubac, I.S. Rončević, M. Metikoš-Huković, R. Babić, M. Petravić, R. Peter, Surface modification of biodegradable magnesium alloys, J. Electrochem. Soc. 159 (2012) 253.
[33] C. Valero Vidal, A. Igual, Mŭnoz, Study of the adsorption process of bovine serum albumin on passivated surfaces of CoCrMo biomedical alloy, Electrochim. Acta 55 (2010) 8445.
[34] A. Igual Muňoz, S. Mischler, Interactive Effects of albumin and phosphate ions on the corrosion of CoCrMo implant alloy, J. Electrochem. Soc. 154 (2007) 562.
[35] A. Kocijan, I. Milosev, D.K. Merl, B. Pihlar, Electrochemical study of Co-based alloys in simulated physiological solution, J. Appl. Electrochem. 34 (2004) 517.
[36] J. Berkowitz, M.G. Inghram, W.A. Chupka, Polymeric gaseous species in the sublimation of molybdenum trioxide, J. Chem. Phys. 26 (1957) 842.
[37] H.E. Evans, Cavity formation and metallurgical changes induced by growth of oxide scale, Mater. Sci. Technol. 4 (1988) 1089.
[38] K.H. Lee, J.K. Yoon, G.H. Kim, J.M. Doh, K.T. Hong, W.Y. Yoon, Growth behavior and microstructure of oxide scale formed on $MoSi_2$ coating at 773 K, J. Mater. Res. 19 (2004) 3009.
[39] F. Zhang, L.T. Zhang, A.D. Shan, J.S. Wu, Oxidation of stoichiometric poly-and single-crystalline $MoSi_2$ at 773 K, Intermetallics 14 (2006) 406.
[40] S. Knittel, S. Mathieu, M. Vilasi, Oxidation behaviour of arc-melted and uniaxial hot pressed $MoSi_2$ at 500 °C, Intermetallics 18 (2010) 2267.
[41] Z. Liu, W. Gao, K.L. Dahm, F. Wang, Oxidation behaviour of sputter-depositedNi–Cr–Al micro-crystalline coatings, Acta Mater. 46 (1998) 1691.
[42] X. Peng, J. Yan, Y. Zhou, F. Wang, Effect of grain refinement on the resistance of 304 stainless steel to breakaway oxidation in wet air, Acta Mater. 53 (2005) 5079.
[43] S. Yang, F. Wang, Z. Sun, S. Zhu, Influence of columnar microstructure of a sputtered NiAl coating on its oxidation behavior at 1000 °C, Intermetallics 10 (2002) 467.